Nanoscale

Accepted Manuscript

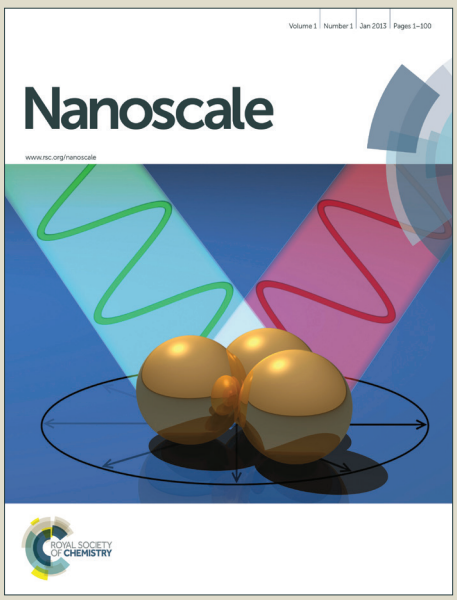

ROYAL SOCIETY OF CHEMISTRY

www.rsc.org/nanoscale

Facile Synthesis, Pharmacokinetic and Systemic Clearance Evaluation, and Positron Emission Tomography Cancer Imaging of ^{64}Cu-Au Alloy Nanoclusters

Yongfeng Zhao, Deborah Sultan, Lisa Detering, Hannah Luehmann, and Yongjian Liu*

Mallinckrodt Institute of Radiology, Washington University School of Medicine, St. Louis, Missouri, 63110, United States

Email: liuyo@mir.wustl.edu

This work was supported in part by a start-up fund from Mallinckrodt Institute of Radiology, Washington University.

Abstract

Gold nanoparticles have been widely used for oncological applications including diagnosis and therapy. However, the non-specific mononuclear phagocyte system accumulation and potential long-term toxicity has significantly limited clinical translation. One strategy to overcome these shortfalls is to reduce the size of gold nanoparticles to allow renal clearance. Herein, we report the preparation of ^{64}Cu alloyed gold nanoclusters (^{64}CuAuNCs) for *in vivo* evaluation of pharmacokinetics, systemic clearance, and positron emission tomography (PET) imaging in a mouse prostate cancer model. The facile synthesis in buffer allowed precisely controlled ^{64}Cu incorporation for high radiolabeling specific activity and stability for sensitive and accurate detection. Through surface pegylation with 350 Da polyethylene glycol (PEG), the ^{64}CuAuNCs-PEG350 afforded optimal biodistribution, significant renal and hepatobiliary excretion. PET imaging showed low non-specific tumor uptake, indicating its potential for active targeting of clinically relevant biomarkers in tumor and metastatic organs.

Keywords: Alloyed gold nanoclusters, cancer imaging, positron emission tomography, radiochemistry, copper-64

Table of contents

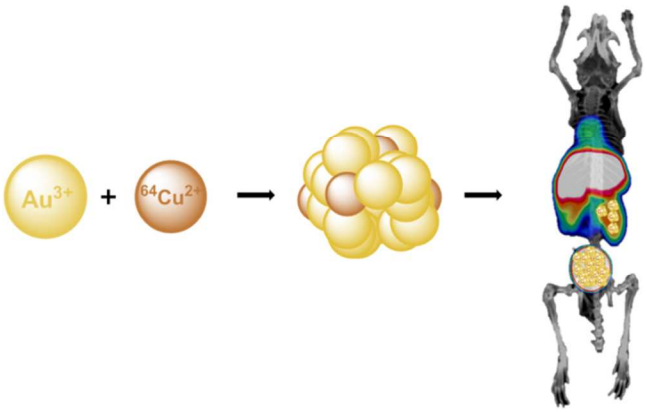

Introduction

Nanoparticles have been widely used in cancer research, including diagnosis and drug delivery for therapy.[1-3] Of various types of nanostructures, gold nanoparticles (AuNPs), such as nanospheres, nanorods, and nanocages, have been widely used for numerous biomedical applications including imaging, drug delivery, and photothermal therapy in a variety of pre-clinical disease models due to their tunable optical properties, biocompatibility, straightforward synthesis, and surface chemistry.[4-6] However, the heavy metal nature of AuNPs normally lead to high non-specific mononuclear phagocyte system (MPS) accumulation *in vivo*, posing significant concern about gene changes and liver necrosis.[7, 8] It has been found that the in vivo toxicity of AuNPs is directly related to their size, shape, surface coating, exposure dose, and administration routes.[9-11] Thus, efforts have been focused on reducing particle toxicity by modulating the physicochemical properties to facilitate translational research of AuNPs.[12]

Of the characteristics of various gold nanoparticles, size plays a dominant role in modulating *in vivo* metabolism. A pioneer study examining the renal excretion efficiency of quantum dots (QDs) with various hydrodynamic (HD) sizes showed that QDs smaller than 5.5 nm was rapidly cleared.[13] In contrast to the variable hepatic clearance, the urinary system proves to be a more reliable metabolism pathway,[12] which propels the development of renal clearable nanoparticles for bionanotechnology.[14-19] Additionally, the effect of surface coatings, especially zwitterionic polymers, on the *in vivo* metabolism of AuNPs has been widely explored.[20, 21] A recent study comparing zwitterionic coating and polyethylene glycol (PEG) showed that zwitterionic material functionalized AuNPs were metabolized much faster than the pegylated counterparts.[22] However, the clinical application of zwitterionic materials needs further demonstration.

Of the biomedical applications using AuNPs, radionuclide-based imaging, such as positron emission tomography (PET), has been a popular topic due to high sensitivity, quantitative determination and translational potential.[23-26] Previously, we have reported the synthesis of ^{64}Cu alloyed AuNPs for cancer positron emission tomography (PET) imaging and revealed improved radiolabel stability and diagnostic accuracy.[27] However, the 27 nm HD size of ^{64}CuAuNPs resulted in high liver and spleen retention albeit PET imaging showed significant tumor accumulation and tumor-to-muscle contrast ratio *via* the enhanced permeation and retention (EPR) effect. In this work, we reported the preparation of renal clearable ^{64}Cu alloyed gold nanoclusters (^{64}CuAuNCs) *via* one-step reaction for *in vivo* biodistribution, clearance, and PET imaging in a mouse PC3 prostate cancer model. This straightforward preparation allowed chelator-free radiolabeling and precise incorporation of ^{64}Cu into the AuNCs' structure at room temperature (RT) with controlled HD sizes. The high specific activity ensured minimal dose administration for sensitive and accurate *in vivo* tumor localization.

Results and discussion

We began the synthesis of copper alloyed gold nanoparticles by mixing non-radioactive $Cu(NO_3)_2$ and $HAuCl_4$ in water, followed by the addition of PEG methyl ether thiol (mPEG-SH).[28] In contrast to previous reports synthesizing Cu alloyed Au nanoparticles,[27, 29] this new approach is more straightforward and time-saving, which is important for preparing molecular probes for PET imaging. Typically, the reaction mixture was added $NaBH_4$ solution with quick stirring for 2 mins and then stirred under RT for 2 h prior to centrifugation. Transmission electron microscopy (TEM) images showed that as-prepared CuAuNCs had uniform distribution with a diameter of 2.5 ± 0.8 nm (Figure 1a). Since pegylation of AuNCs has been demonstrated as an effective strategy in preventing AuNPs serum protein adsorption in vivo, five mPEG-SH

with molecular weights of 350 Da, 550 Da, 750 Da, 1000 Da, and 3000 Da were used for surface modification to systemically study the renal clearance efficiency of CuAuNCs).[30] As shown in Table 1, of the five candidates, both CuAuNCs-PEG350 and CuAuNCs-PEG550 had HD sizes characterized by dynamic light scattering less than 5.5 nm, while CuAuNCs-PEG750 had HD size similar to the kidney filtration threshold.[31] For CuAuNCs pegylated with 1000 Da and 3000 Da PEG, sizes were both above the 5.5 nm threshold. Interestingly, the surface charges of the five pegylated CuAuNCs decreased with the increase of PEG chain lengths, although most of them had close to neutral surface charge (-10 mV to 10 mV) except for the slightly negatively charged CuAuNCs-PEG3000 (-15.6 ± 0.10) (Table 1), which was consistent with previous reports that surface pegylation with thio-containing PEG shielded the negative charge of gold nanoparticles.[32, 33] Owing to their ultrasmall sizes, all five nanoclusters showed weak UV absorption between 550 nm and 600 nm (Figure 1b).[11, 15]

The preparation of ^{64}CuAuNCs was performed following the same procedure for synthesizing non-radioactive CuAuNCs by replacing $Cu(NO_3)_2$ with $^{64}CuCl_2$. After purification, the representative instant radioactive thin-layer chromatography (radio-TLC) showed one single peak (Figure 1c), indicating 100% radiochemical purity. Importantly, with increasing $^{64}CuCl_2$ precursor activity, the specific activity of ^{64}CuAuNCs-PEG350 increased linearly (Figure 1d). When 67 MBq of $^{64}CuCl_2$ was used, the specific activity of ^{64}CuAuNCs-PEG350 was 14.3 MBq/nmol, ensuring trace amount (3.7 MBq (0.25 nmol)/dose) administration for *in vivo* PET imaging. Actually, this specific activity gave rise to one ^{64}Cu in every 5.08×10^5 Au atoms.[34] In our synthesis of CuAuNCs-PEG350 using non-radioactive Cu, the percent composition of Cu atom could be up to 80% as determined by inductively coupled plasma-mass spectrometry. Given the presence of non-radioactive Cu in the $^{64}CuCl_2$ solution,[34] there is still great potential

(up to 2.0×10^4 fold) to increase the specific activity of ^{64}CuAuNCs-PEG350 although practical considerations and alterations in the radioactive nanoclusters produced might limit the degree to which this increase could be fully realized. Herein, this study is to demonstrate the straightforward synthesis of ^{64}CuAuNCs for improved pharmacokinetics and clearance profile comparing to our previous study using HD of 27 nm ^{64}CuAuNPs.[27] This facile, one-step preparation strategy can also be used to prepare targeted ^{64}CuAuNCs *via* the conjugation of targeting moieties, such as peptides for further oncological applications. Importantly, the fast synthesis and high specific activity of ^{64}CuAuNCs would require ultra-trace amount administration for *in vivo* applications, which could substantially decrease any potential toxicity effect raised by the dosage of injected nanoparticles.[11, 12, 17]

It is well established that nanoparticle size, composition and surface properties play a significant role in a number of physiological parameters such as biodistribution, kidney excretion, hepatic filtration, tissue extravasation, and diffusion.[35] Given the well-defined sizes of the five pegylated ^{64}CuAuNCs (Table 1), we chose ^{64}CuAuNCs-PEG350 and ^{64}CuAuNCs-PEG1000 with HD sizes smaller (4.29 ± 0.15 nm) and bigger (6.90 ± 0.48 nm) than the 5.5 nm renal clearance threshold to study their *in vivo* pharmacokinetics and clearance profiles. As shown in Figures 2 and S1, both ^{64}CuAuNCs-PEG350 and ^{64}CuAuNCs-PEG1000 showed similar organ distribution trends during the 24 h studies. Compared to the short blood retention of ^{64}CuAuNCs-PEG350 ($t_{1/2}$ = 0.87 h), the half-life of ^{64}CuAuNCs-PEG1000 ($t_{1/2}$ = 2.62 h) in blood circulation was two times longer owing to the effect of PEG chain length. This was also revealed by the tracer uptake in other blood pool organs such as heart and lung and in agreement with another report using comparable size of AuNCs despite the difference of mouse species.[22] In contrast to the 27 nm ^{64}CuAuNPs (liver: 42.9 ± 3.44 %ID/g, spleen: 203 ± 11.1% ID/g) previously reported at 24 h

post injection (p.i.),[27] the liver accumulations of ^{64}CuAuNCs-PEG350 (14.5 ± 2.68 %ID/g, p<0.0001, n=4/group) and ^{64}CuAuNCs-PEG1000 (22.1 ± 3.62 %ID/g, p<0.0002, n=4/group) were 66.3% and 48.5% reduced, respectively. Importantly, the spleen uptake was almost two orders of magnitude decreased for ^{64}CuAuNCs-PEG350 (spleen: 2.12 ± 0.54 %ID/g, 94.8 fold, p<0.0001, n=4/group) and 50.8 fold dropped for ^{64}CuAuNCs-PEG1000 (spleen: 3.92 ± 0.85%ID/g, p<0.0001, n=4/group), confirming the substantial effect size plays in the accumulation of nanoparticles through MPS.[36] Further, these two pegylated ^{64}CuAuNCs showed much lower MPS uptake than those obtained with non-pegylated AuNCs but comparable accumulation to glutathione coated AuNCs of similar sizes.[11, 37, 38] This was consistent with a previous report demonstrating the effects of surface modification on AuNCs' *in vivo* pharmacokinetics.[39]

Interestingly, both ^{64}CuAuNCs showed gradually decreased MPS localization during the 24 h period. This differed from the large AuNPs in various shapes which showed constant hepatic/splenic retentions.[25, 27, 40, 41] Further, a substantial gastrointestinal (GI) tract (stomach and intestine) clearance was observed at each time point (Figure 2), which was much higher than those obtained with AuNCs of similar sizes.[11, 22, 42] This excretion pattern was in agreement with the hepatobiliary clearance of ^{64}CuAuNCs-PEG350 (4.8%, 26.5%, and 36.2% of injected dose at 4 h, 24 h, and 48 h p.i., respectively) and ^{64}CuAuNCs-PEG1000 (1.8%, 34.0%, and 38.4% of injected dose at 4 h, 24 h, and 48 h p.i., respectively) observed in the feces (Figure 3). It is known that hepatocytes are within the pathway for biliary excretion and therefore particles processed by these cells are potentially excreted into the bile for fecal clearance. Alternatively, Kupffer cells are part of the MPS system and rely exclusively on intracellular degradation for particle removal. Particles that are not broken down by intracellular processes will remain within

the cell and will therefore be retained by the organ. Given the stability of this alloyed nanostructure as previously demonstrated,[27] it would be reasonable to assume that the two ^{64}CuAuNCs were most likely endocytosed by hepatocytes rather than Kupffer cells during the systemic circulation. Further, it is worthwhile to point out that although the MPS accumulation in this study was a quick process, the hepatobiliary excretion was relatively slow.[30] Most clearance was observed at 24 h p.i. while a significant amount was still observed at 48 h for both ^{64}CuAuNCs. In contrast to the hepatobiliary clearance data obtained with AuNPs in various sizes reviewed elsewhere,[39] the results reported here were much higher. However, due to the complex effect of animal physiological conditions and the nanoparticles' physicochemical parameters, the *in vivo* hepatobiliary transport mechanism for the two ^{64}CuAuNCs reported herein needs further investigation.

In contrast to the complex, lengthy, and unpredictable clearance through the hepatobiliary system, the fast, efficient, and controllable renal excretion is a desirable pathway for various nanoclusters' *in vivo* applications. As previously reported, renal clearance of intravascular agents is a multifaceted process involving glomerular filtration, tubular secretion, and finally elimination of the molecules through urinary excretion.[30] Of various factors affecting the excretion efficiency, the HD size is the most critical parameter with a filtration-size threshold reported around 5.5 - 6 nm.[39] As shown in figure 3, owing to the distinct sizes of the two nanoclusters, the accumulative renal clearance of ^{64}CuAuNCs-PEG350 (27.0%, 31.4%, and 40.8% of injected dose at 4 h, 24 h, and 48 h p.i., respectively) was significantly ($P < 0.0001$, n=4/group) higher than that obtained with ^{64}CuAuNCs-PEG1000 (1.94%, 6.73%, and 7.86% of injected dose at 4 h, 24 h, and 48 h p.i., respectively) at each time point. In contrast to the slow clearance through feces, the majority of ^{64}CuAuNCs-PEG350 was excreted within the first 4 hours,

consistent with other reports irrespective of the surface coating.[11, 15, 17, 22] Due to the intermediate HD size of ^{64}CuAuNCs-PEG1000, some low renal clearance was also observed throughout the study (Figure 3).[15, 30]

Nanoparticle toxicity has been an interesting and active topic along the development of nanobiotechnology due to the long-term accumulation, unclear excretion pathway, and complex *in vivo* interactions regardless of the composition of the nanoparticles.[43-45] In contrast to the large AuNPs, AuNCs have less concern mainly due to the lower MPS accumulation. However, their high accumulation in renal system raised significant considerations about the potential effects given the fact that these particles could effectively enter the renal cells.[46] Even though AuNCs may not lead to nephropathy caused by gold salt,[47] their effects on tubular degeneration, necrosis, and glomerulonephritis need thorough pathological examination. Alternatively, one effective strategy to minimize toxicity concerns is to lower the dosage of AuNCs. In this study, the high specific activity of ^{64}CuAuNCs enabled the trace amount (0.25 nmol) administration for PET imaging (0.025 nmol for biodistribution), which was at least two orders of magnitude less than the amount of AuNCs used in other studies.[17, 38, 48] Importantly, the specific activity of ^{64}CuAuNCs could be further improved as discussed above for minimal amount *in vivo* administration, indicating its great potential for cancer imaging.

We next studied the imaging capability of ^{64}CuAuNCs-PEG350 and ^{64}CuAuNCs-PEG1000 in a mouse PC3 prostate cancer model using a small animal PET/CT system. As shown in Figure 4, both ^{64}CuAuNCs showed fast clearance from systemic circulation and major retention in the MPS system. Consistent with the biodistribution data, ^{64}CuAuNCs-PEG350 PET imaging demonstrated substantial renal excretion at 1 h and 4 h p.i. while ^{64}CuAuNCs-PEG1000 showed minimal renal clearance. At 24 h p.i., both ^{64}CuAuNCs showed substantial GI tract accumulation.

Interestingly, neither ^{64}CuAuNCs showed noticeable tumor retention until 24 h p.i. despite the active tumor angiogenesis as shown in figure S2. The quantitative uptake analysis showed gradually increased tracer accumulation in tumors from ~ 0.8 %ID/g at 1 h to ~3 %ID/g at 24 h p.i.. Both were ~ 5 fold less than that obtained with the 27 nm ^{64}CuAuNPs and significantly lower than the data acquired with 5.5 nm AuNCs in mouse breast cancer models (~ 8 %ID/g).[22, 27] Interestingly, the tumor uptake was similar to the data obtained with 3 nm AuNCs coated with zwitterionic glutathione (2.3%ID/g at 12 h), which are known for faster clearance than their pegylated counterparts.[48] Due to the low tumor retention, the tumor-to-muscle contrast ratios were also significantly ($p<0.001$, n=4/group) less that that obtained with the large ^{64}CuAuNPs.[27] Further analysis of the intratumoral distribution of these ^{64}CuAuNCs with autoradiography imaging demonstrated heterogeneous distribution of radioactivity across the tumor mass (Figure 5), which was in agreement with the PET images.

In nanoparticle cancer imaging, the EPR effect has been widely used for tumor delivery due to the leaky vasculature in tumors and metastatic organs.[6, 49, 50] Recently, there are more studies focusing on the active targeting for specific detection of biomarkers related to the physiological conditions during tumor progression, which will provide useful information for tumor staging and treatment.[51] However, due to the significant contribution of non-specific retention in tumors caused by the EPR effect when compared to the overall imaging efficiency, nanoparticle imaging methods need to significantly improve detection specificity to provide an accurate read-out about the variation of tumor biology for clinical translation. Thus, a nanostructure with low non-specific uptake may be an ideal candidate nanoplatform for further evaluation in targeted tumor imaging. Due to their high specific activity, efficient systemic clearance, and low non-specific retention in tumors, the two ^{64}CuAuNCs, especially ^{64}CuAuNCs-PEG350, developed in this

study have great potential for sensitive, specific detection of clinically relevant tumor biomarkers and will be useful tools for cancer staging and metastasis detection.

Conclusion

In summary, we have developed a new renal clearable, ^{64}Cu alloyed gold nanocluster for cancer imaging through a facile one-step preparation strategy. By varying the initial activity of $^{64}CuCl_2$ precursor integrated into the structure of AuNCs we were able to freely control the radiolabeling specific activity, thus creating a sensitive PET imaging probe for cancer detection with minimal dose administration. The well-defined size led to rapid systematic clearance, low MPS accumulation, and significant renal and hepatobiliary clearance. PET/CT imaging showed low non-specific tumor retention and heterogeneous intratumoral distribution. Although current studies focus on the *in vivo* evaluation of non-targeted ^{64}CuAuNCs-PEG350, the understanding of its in vivo pharmacokinetics, clearance, and PET imaging capability will help us to design next targeted nanoprobe for specific cancer imaging. The demonstration of fast, controlled radiosynthesis of nanoclusters in tunable HD sizes will serve as a point of entry for a broader range of biomedical applications utilizing radiometal-alloyed nanostructures in pre-clinical and translational research.

Materials and methods

Chemicals. Hydrochloric acid (HCl, 37%, TraceSELECT®), nitric acid (HNO_3, 70%, ≥ 99.999% trace metals basis), chloroauric aicd ($HAuCl_4$ $3H_2O$, 99.999%), copper nitrate ($Cu(NO_{3)2}$, 99.999% trace metals basis) were all obtained from Sigma-Aldrich (St. Louis, MO) and used as received. Water with a resistivity of 18.2 MΩ cm was prepared using an E-Pure filtration system from Barnstead International (Dubuque, IA). Poly(ethylene glycol) methyl ether thiol (HS-PEG-OCH_3,

Mw ≈ 350, 550, 750, 1000, and 3000) were purchased from Nanocs (Boston, MA) and used as received.

Synthesis of Non-radioactive CuAu Nanoclusters. In a typical reaction, water (1.0 mL), $HAuCl_4$ (10 mM, 94 μL), and $Cu(NO_3)_2$ (10 mM, 94 μL) were mixed in a glass vial, followed by the dropwise addition of mPEG-thiol (MW=350/550/ 750/1000/3000 Da, 10 mM, 200 μL). The mixture was added sodium borohydride (20 mM, 200 μL) under quick stirring for 2 min at room temperature and then kept for 2 hours. The CuAu nanoclusters (CuAuNCs) were purified by using centrifuge filter (Amicon, 10K) and washed by MilliQ water three times.

Synthesis of ^{64}CuAuNCs. ^{64}CuAuNCs were prepared following the same procedure as preparing non-radioactive CuAu nanoclusters. Instead of adding $Cu(NO_3)_2$, radioactive $^{64}CuCl_2$ (157 MBq) was added. The synthesized ^{64}CuAuNCs was challenged with ethylenediaminetetraacetic acid (EDTA, 10 mM in neutral 50 mM phosphate buffer, 5 μL) and then purified by an centrifuge filter (Amicon, 10K). The radiochemical purity was determined by instant radio-thin layer chromatography (Radio-TLC).

Characterizations of CuAuNCs and ^{64}CuAuNCs. The UV-Vis absorption spectra are recorded by a Cary 60 UV-Vis spectrometer (Agilent Technologies, Santa Clara, CA). The gold nanoclusters were examined using a Tecnai G2 Spirit transmission Electron Microscope (TEM) operated at 120 kV (FEI, Hillsboro, OR). Dynamic light scattering (NanoZS, Malvern, Worcestershire, UK) was performed to measure the hydrodynamic diameter and zeta-potential. The concentration of Au and Cu in the alloyed nanoclusters was measured by Elan DRC II inductively coupled plasma mass spectrometry (ICP-MS, Perkin-Elmer, Waltham, MA).

Animal Biodistribution Studies. All animal studies were performed in compliance with guidelines set forth by the NIH Office of Laboratory Animal Welfare and approved by the

Washington University Animal Studies Committee. The normal male C57BL/6 mice (Charles River Laboratory, Wilmington, MA) were used for the biodistribution studies. About 370 kBq of ^{64}CuAuNCs in 100 μL saline (APP pharmaceuticals, Schaumburg, IL) was injected *via* the tail vein. The mice were anesthetized with inhaled isoflurane and re-anesthetized before euthanizing them by cervical dislocation at each time point (1 h, 4 h, and 24 h post injection, n=4/group). Organs of interest were collected, weighed, and counted in a well Beckman 8000 gamma counter (Beckman, Fullterton, CA). Standards were prepared and measured along with the samples to calculate percentage of the injected dose per gram of tissue (%ID/g) and percentage of injected dose per organ (%ID/organ).

Clearance Studies. The clearance profile of ^{64}CuAuNCs was evaluated by measuring the radioactivity in the urine and feces samples collected during the study. A group of mice (n=4/group) were housed in a metabolism study cage where the urine and feces were separately collected at 4 h, 24 h, and 48 h post ^{64}CuAuNCs injection (370kBq/animal). The gamma counting results were calculated as mean percentage of injected dose (%ID).

Micro-PET/CT Imaging. The human prostate cancer PC3 cell line (ATCC, Manassas, VA) was cultured in RPMI 1640 medium supplemented with 10% FCS, 50 units/mL sodium penicillin, 50 units/mL streptomycin sulfate, and 2 mM L-glutamine at 37 ºC with 5% CO_2. Male athymic nu/nu mice at 6 weeks age (Charles River Laboratory, Wilmington, MA) were subcutaneously implanted with 3×10^6 PC3 cells into the right flank. The tumors were allowed to grow for 5 weeks to reach a size of approximately 0.5 – 0.8 g before the mice were used for the PET/CT imaging studies. Mice were anesthetized with isoflurane and injected with 3.7 MBq of ^{64}CuAuNCs in 100 μL of saline *via* the tail vein. MicroPET scans were performed on either microPET Focus 220 (Siemens, Malvern, PA) or Inveon PET/CT system (Siemens, Malvern, PA)

at 1 hour (20 min frame), 4 hour (30 min frame), and 24 hour post-injection (60 min frame). The microPET images were corrected for attenuation, scatter, normalization, and camera dead time and co-registered with microCT images. All of the PET scanners were cross-calibrated periodically. The microPET images were reconstructed with the maximum a posteriori (MAP) algorithm and analyzed by Inveon Research Workplace. The tumor uptake of ^{64}CuAuNCs was calculated in terms of the percent injected dose per gram (%ID/g) of tumor tissue in three-dimensional regions of interest (ROIs) without the correction for partial volume effect.

Autoradiography Studies. After PET/CT scan, tumors were excised and frozen in Optimal Cutting Temperature (O.C.T.) Compound and then 8 – 20 slices of 50 μm thickness were cut with a Vibratome 8850 whole body cryo-microtome (SIMS Co., Ltd., Tokyo, Japan). Tumor slices were placed on glass slides for 2D autoradiography using an InstantImager Electronic Autoradiography instrument (Packard, Meriden, CT). Images were acquired and analyzed with Imager software (Packard, Meriden, CT).

Histopathology. Tumor specimens were embedded in paraffin and step-sectioned (10 mm) transversely at 1-mm intervals. The sections were deparaffinized and stained with hematoxylin and eosin stain.

Statistical analysis. Group variation is described as mean ± SD. Groups were compared using 1-way ANOVA with a Bonferroni posttest. Individual group differences were determined with use of a 2-tailed Mann–Whitney test. The significance level in all tests was $P \leq 0.05$. Prism, version 6.04 (GraphPad), was used for all statistical analyses.

Conflict of Interest: The authors declare no competing financial interest.

References

1. E. K. Chow and D. Ho, *Sci Transl Med*, 2013, 5, 216rv214.
2. M. Ferrari, *Nat. Rev. Cancer*, 2005, 5, 161-171.
3. O. C. Farokhzad and R. Langer, *ACS Nano*, 2009, 3, 16-20.
4. D. A. Giljohann, D. S. Seferos, W. L. Daniel, M. D. Massich, P. C. Patel and C. A. Mirkin, *Angew. Chem. Int. Ed. Engl.*, 2010, 49, 3280-3294.
5. A. J. Mieszawska, W. J. Mulder, Z. A. Fayad and D. P. Cormode, *Mol. Pharm.*, 2013, 10, 831-847.
6. D. Kumar, N. Saini, N. Jain, R. Sareen and V. Pandit, *Expert Opin Drug Deliv*, 2013, 10, 397-409.
7. W. S. Cho, M. Cho, J. Jeong, M. Choi, B. S. Han, H. S. Shin, J. Hong, B. H. Chung and M. H. Cho, *Toxicol. Appl. Pharmacol.*, 2010, 245, 116-123.
8. J. Lipka, M. Semmler-Behnke, R. A. Sperling, A. Wenk, S. Takenaka, C. Schleh, T. Kissel, W. J. Parak and W. G. Kreyling, *Biomaterials*, 2010, 31, 6574-6581.
9. W. Jiang, B. Y. Kim, J. T. Rutka and W. C. Chan, *Nat Nanotechnol*, 2008, 3, 145-150.
10. Y. Pan, A. Leifert, D. Ruau, S. Neuss, J. Bornemann, G. Schmid, W. Brandau, U. Simon and W. Jahnen-Dechent, *Small*, 2009, 5, 2067-2076.
11. X. D. Zhang, D. Wu, X. Shen, P. X. Liu, F. Y. Fan and S. J. Fan, *Biomaterials*, 2012, 33, 4628-4638.
12. H. S. Choi, W. Liu, F. Liu, K. Nasr, P. Misra, M. G. Bawendi and J. V. Frangioni, *Nat Nanotechnol*, 2010, 5, 42-47.
13. H. S. Choi, W. Liu, P. Misra, E. Tanaka, J. P. Zimmer, B. Itty Ipe, M. G. Bawendi and J. V. Frangioni, *Nat. Biotechnol.*, 2007, 25, 1165-1170.

14. J. Liu, M. Yu, C. Zhou and J. Zheng, *Mater. Today*, 2013, 16, 477-486.

15. C. Alric, I. Miladi, D. Kryza, J. Taleb, F. Lux, R. Bazzi, C. Billotey, M. Janier, P. Perriat, S. Roux and O. Tillement, *Nanoscale*, 2013, 5, 5930-5939.

16. B. H. Kim, M. J. Hackett, J. Park and T. Hyeon, *Chem. Mater.*, 2014, 26, 59-71.

17. C. A. Simpson, K. J. Salleng, D. E. Cliffel and D. L. Feldheim, *Nanomedicine*, 2013, 9, 257-263.

18. F. Lux, A. Mignot, P. Mowat, C. Louis, S. Dufort, C. Bernhard, F. Denat, F. Boschetti, C. Brunet, R. Antoine, P. Dugourd, S. Laurent, L. Vander Elst, R. Muller, L. Sancey, V. Josserand, J. L. Coll, V. Stupar, E. Barbier, C. Remy, A. Broisat, C. Ghezzi, G. Le Duc, S. Roux, P. Perriat and O. Tillement, *Angew. Chem. Int. Ed. Engl.*, 2011, 50, 12299-12303.

19. D. Kryza, J. Taleb, M. Janier, L. Marmuse, I. Miladi, P. Bonazza, C. Louis, P. Perriat, S. Roux, O. Tillement and C. Billotey, *Bioconjugate Chem.*, 2011, 22, 1145-1152.

20. X. Liu, H. Huang, G. Liu, W. Zhou, Y. Chen, Q. Jin and J. Ji, *Nanoscale*, 2013, 5, 3982-3991.

21. N. T. K. Thanh and G. L. A. W., *Nano Today*, 2010, 5, 213-230.

22. J. Liu, M. Yu, X. Ning, C. Zhou, S. Yang and J. Zheng, *Angew. Chem. Int. Ed. Engl.*, 2013, 52, 12572-12576.

23. K. Cheng, S. R. Kothapalli, H. Liu, A. L. Koh, J. V. Jokerst, H. Jiang, M. Yang, J. Li, J. Levi, J. C. Wu, S. S. Gambhir and Z. Cheng, *J. Am. Chem. Soc.*, 2014, 136, 3560-3571.

24. Z. Zhang, Y. Liu, C. Jarreau, M. J. Welch and J. S. Taylor, *Biomater Sci*, 2013, 1, 1055-1064.

25. Y. Wang, Y. Liu, H. Luehmann, X. Xia, P. Brown, C. Jarreau, M. Welch and Y. Xia, *ACS Nano*, 2012, 6, 5880-5888.

26. Y. Liu and M. J. Welch, *Bioconjug. Chem.*, 2012, 23, 671-682.

27. Y. Zhao, D. Sultan, L. Detering, S. Cho, G. Sun, R. Pierce, K. L. Wooley and Y. Liu, *Angew. Chem. Int. Ed. Engl.*, 2014, 53, 156-159.

28. C. M. Andolina, A. C. Dewar, A. M. Smith, L. E. Marbella, M. J. Hartmann and J. E. Millstone, *J. Am. Chem. Soc.*, 2013, 135, 5266-5269.

29. C. H. Su, H. S. Sheu, C. Y. Lin, C. C. Huang, Y. W. Lo, Y. C. Pu, J. C. Weng, D. B. Shieh, J. H. Chen and C. S. Yeh, *J. Am. Chem. Soc.*, 2007, 129, 2139-2146.

30. M. Longmire, P. L. Choyke and H. Kobayashi, *Nanomedicine (Lond)*, 2008, 3, 703-717.

31. W. M. Deen, M. J. Lazzara and B. D. Myers, *Am J Physiol Renal Physiol*, 2001, 281, F579-596.

32. W. Wang, Q. Q. Wei, J. Wang, B. C. Wang, S. H. Zhang and Z. Yuan, *J. Colloid Interface Sci.*, 2013, 404, 223-229.

33. E. C. Cho, Q. Zhang and Y. Xia, *Nat Nanotechnol*, 2011, 6, 385-391.

34. W. P. Wuelfing, S. M. Gross, D. T. Miles and R. W. Murray, *J. Am. Chem. Soc.*, 1998, 120, 12696-12697.

35.R. Kumar, I. Roy, T. Y. Ohulchanskky, L. A. Vathy, E. J. Bergey, M. Sajjad and P. N. Prasad, *ACS Nano*, 2010, 4, 699-708.

36. S. Nagayama, K. Ogawara, Y. Fukuoka, K. Higaki and T. Kimura, *Int. J. Pharm.*, 2007, 342, 215-221.

37. M. Semmler-Behnke, W. G. Kreyling, J. Lipka, S. Fertsch, A. Wenk, S. Takenaka, G. Schmid and W. Brandau, *Small*, 2008, 4, 2108-2111.

38. C. Zhou, M. Long, Y. Qin, X. Sun and J. Zheng, *Angew. Chem. Int. Ed. Engl.*, 2011, 50, 3168-3172.

39. J. P. Almeida, A. L. Chen, A. Foster and R. Drezek, *Nanomedicine (Lond)*, 2011, 6, 815-835.

40. Y. Wang, Y. Liu, H. Luehmann, X. Xia, D. Wan, C. Cutler and Y. Xia, *Nano Lett.*, 2013, 13, 581-585.

41. Y. Wang, K. C. Black, H. Luehmann, W. Li, Y. Zhang, X. Cai, D. Wan, S. Y. Liu, M. Li, P. Kim, Z. Y. Li, L. V. Wang, Y. Liu and Y. Xia, *ACS Nano*, 2013, 7, 2068-2077.

42. X. D. Zhang, J. Chen, Z. Luo, D. Wu, X. Shen, S. S. Song, Y. M. Sun, P. X. Liu, J. Zhao, S. Huo, S. Fan, F. Fan, X. J. Liang and J. Xie, *Adv Healthc Mater*, 2014, 3, 133-141.

43. A. Nemmar, J. A. Holme, I. Rosas, P. E. Schwarze and E. Alfaro-Moreno, *Biomed Res Int*, 2013, 2013, 279371.

44. P. Kovacic and R. Somanathan, *Methods Mol. Biol.*, 2013, 1028, 15-35.

45. J. Ai, E. Biazar, M. Jafarpour, M. Montazeri, A. Majdi, S. Aminifard, M. Zafari, H. R. Akbari and H. G. Rad, *Int. J. Nanomedicine*, 2011, 6, 1117-1127.

46. A. Sereemaspun, R. Rojanathanes and V. Wiwanitkit, *Ren. Fail.*, 2008, 30, 323-325.

47. T. T. Antonovych, *Ann. Clin. Lab. Sci.*, 1981, 11, 386-391.

48. J. Liu, M. Yu, C. Zhou, S. Yang, X. Ning and J. Zheng, *J. Am. Chem. Soc.*, 2013, 135, 4978-4981.

49. D. M. McDonald and P. Baluk, *Cancer Res.*, 2002, 62, 5381-5385.

50. S. M. Weis, *Curr. Opin. Hematol.*, 2008, 15, 243-249.

51. U. Prabhakar, H. Maeda, R. K. Jain, E. M. Sevick-Muraca, W. Zamboni, O. C. Farokhzad, S. T. Barry, A. Gabizon, P. Grodzinski and D. C. Blakey, *Cancer Res.*, 2013, 73, 2412-2417.

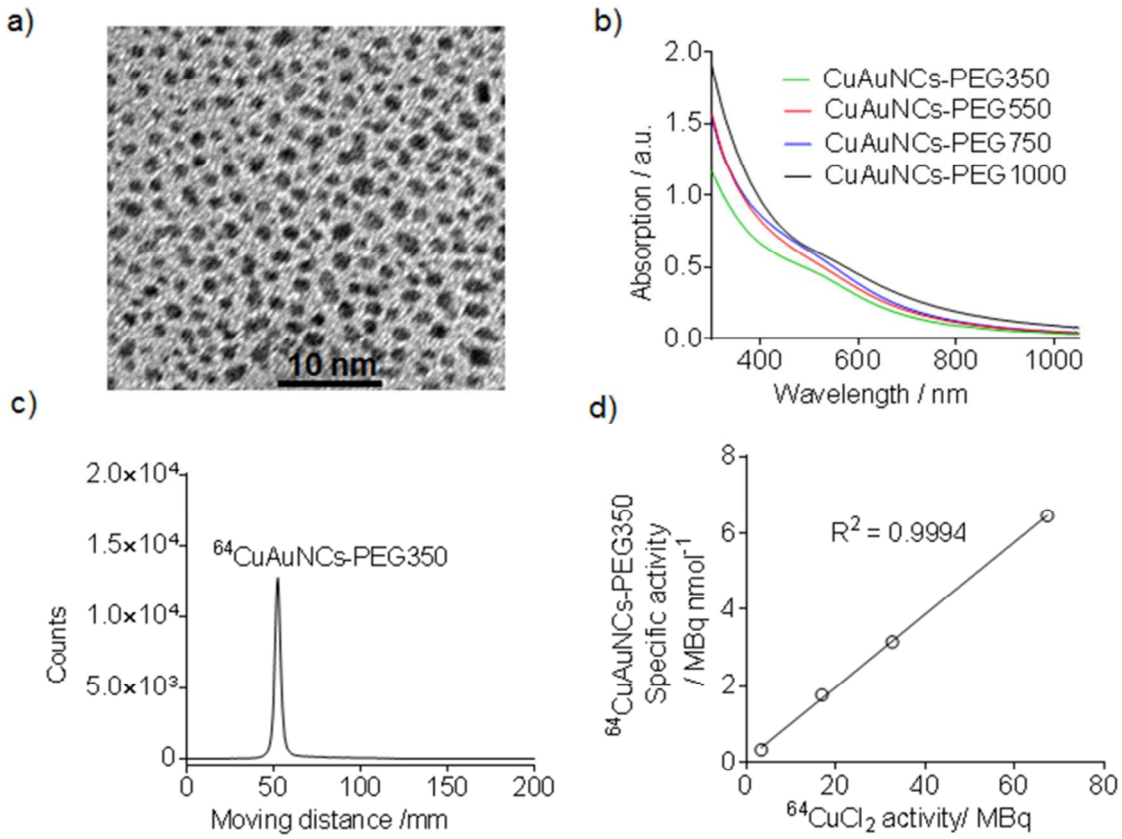

Figure 1. a) TEM image of the alloyed ^{64}CuAuNCs (diameter: 2.8 ±0.8 nm) after decay. Scale bar: 10 nm. b) Normalized UV spectra of CuAuNCs pegylated with four different lengths of PEG. c) radio-TLC profile of ^{64}CuAuNCs-PEG350. d) Correlation of the radioactivity of the $^{64}CuCl_2$ precursor and specific activity of ^{64}CuAuNCs-PEG350.

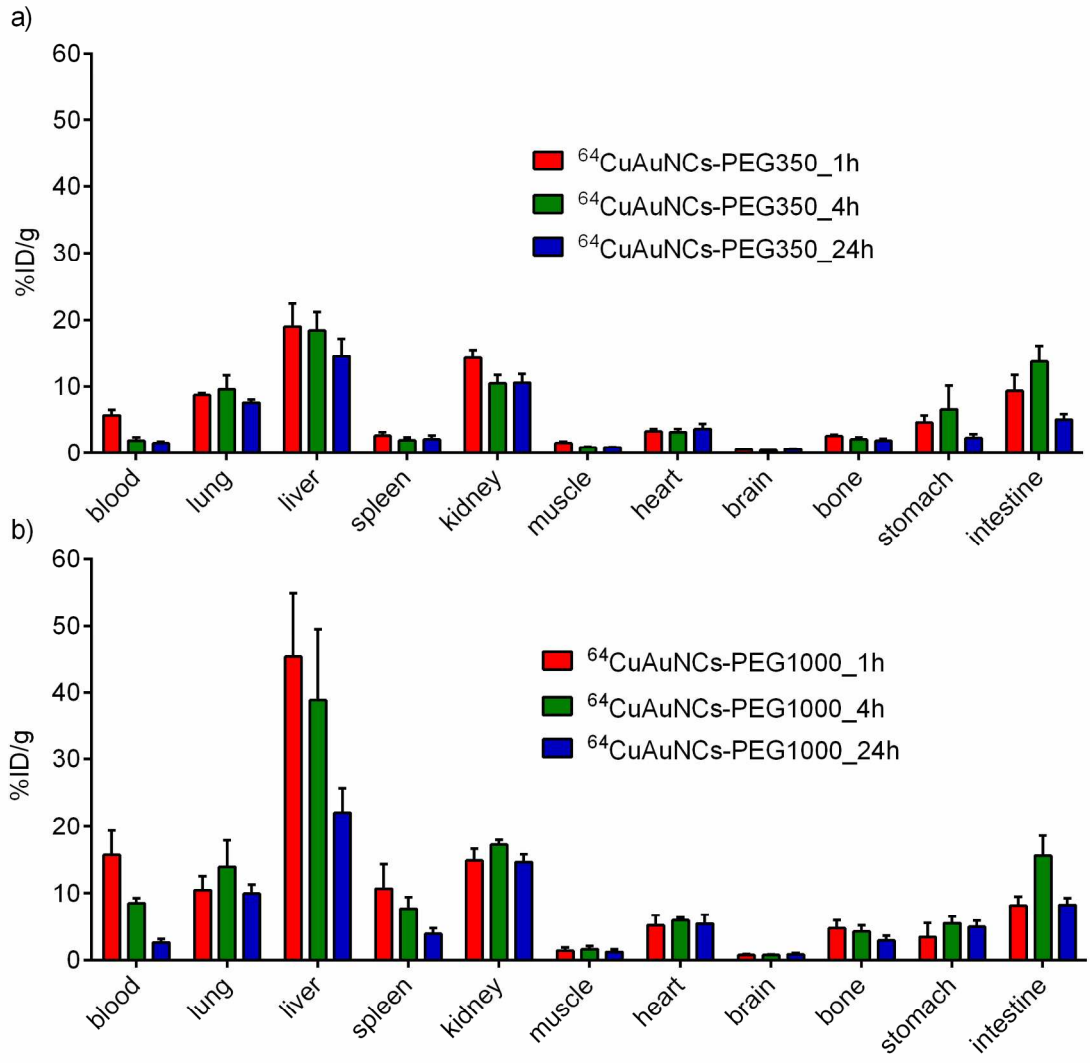

Figure 2. Biodistribution of alloyed a) ^{64}CuAuNCs-PEG350 and b) ^{64}CuAuNCs-PEG1000 in wild-type C57BL/6 male mice at 1 h, 4 h, and 24 h post injection (n=4/group).

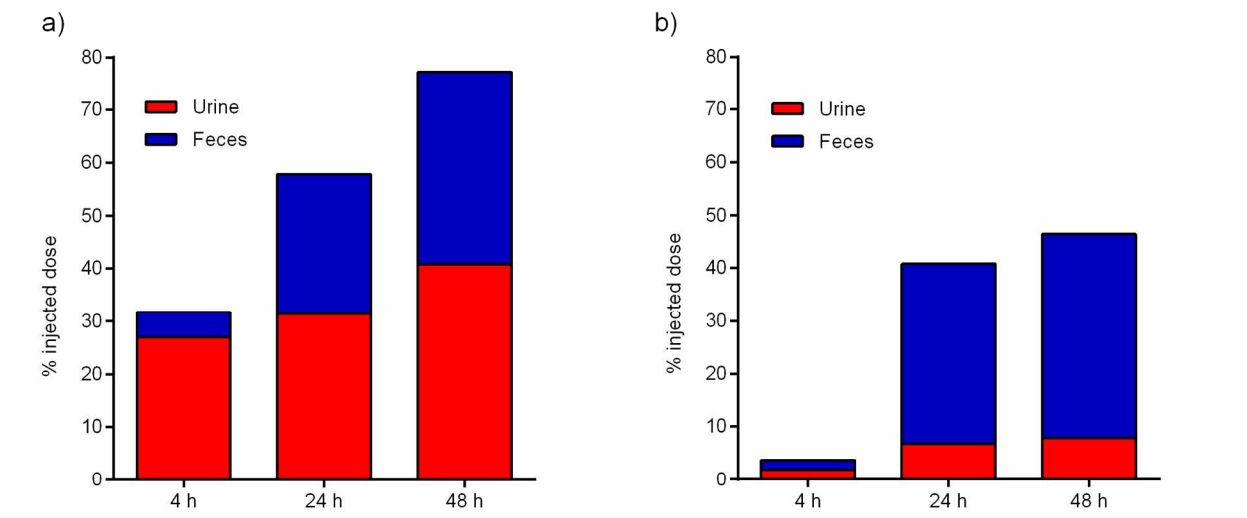

Figure 3. Clearance profiles of a) ^{64}CuAuNCs-PEG350 and b) ^{64}CuAuNCs-PEG1000 in wild-type C57BL/6 male mice after intravenous injection.

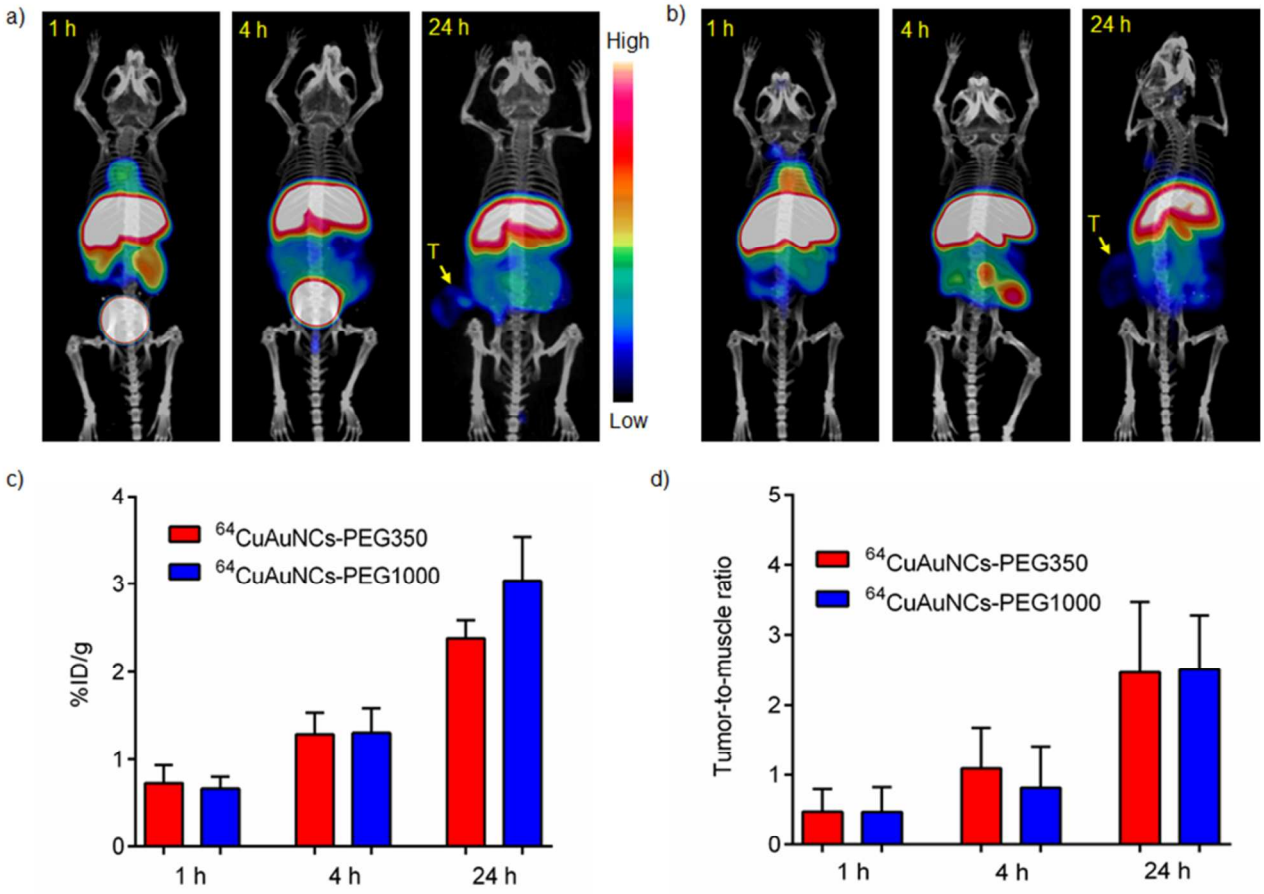

Figure 4. Representative PET/CT images at 1 h, 4 h, and 24 h post injection of a) ^{64}CuAuNCs-PEG350, b) ^{64}CuAuNCs-PEG1000 in PC3 tumor bearing mice (T: tumor). c) Quantitative tumor uptake of ^{64}CuAuNCs-PEG350 and ^{64}CuAuNCs-PEG1000 in PC3 tumor bearing mice. d) Tumor-to-muscle ratio of ^{64}CuAuNCs-PEG350 and ^{64}CuAuNCs-PEG1000 in PC3 tumor bearing mice.

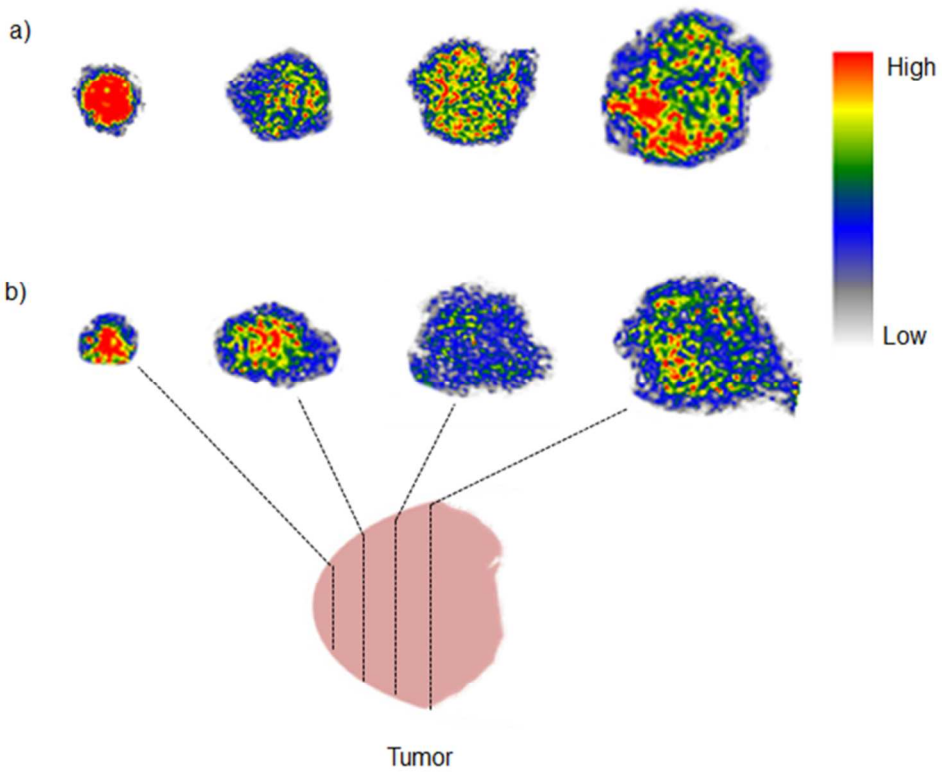

Figure 5. Representative autoradiography of alloyed a) ^{64}CuAuNCs-PEG350 and b) ^{64}CuAuNCs-PEG1000 in PC3 tumor at 48 h post injection showing the heterogeneous intratumoral distribution.

Table 1. Hydrodynamic size distribution and zeta potential of CuAuNCs pegylated with various lengths of PEGs determined by dynamic light scattering

Samples	PEG350	PEG550	PEG750	PEG1000	PEG3000
Number (nm)	4.29±0.15	5.17±0.34	5.58±0.28	6.90±0.48	10.46±0.24
Volume (nm)	5.69±0.30	8.61±1.33	8.77±2.05	9.45±2.65	164.7±211.8
Intensity (nm)	286.8±99.42	593.0±114.7	242.6±73.00	357.0±166.6	896.9±849.6
Zeta potential (mV)	10.3±2.56	-3.66±1.50	-7.22±2.30	-8.31±1.58	-15.6±0.10